A multiscale peridynamic framework for modelling mechanical properties of polymer-based nanocomposites

Greta Ongaro[a,b,*], Roberta Bertani[c], Ugo Galvanetto[a,b], Alessandro Pontefisso[d], Mirco Zaccariotto[a,b]

[a]*Centre of Studies and Activities for Space (CISAS) - "G. Colombo", v. Venezia 15, Padova 35131, Italy*
[b]*Department of Industrial Engineering, University of Padova, v. Venezia 1, Padova 35131, Italy*
[c]*Department of Industrial Engineering, University of Padova, v. F. Marzolo 9, Padova 35131, Italy*
[d]*Department of Management and Engineering, University of Padova, Stradella San Nicola 3, Vicenza 36100, Italy*

Abstract

In this work, a peridynamics-based representative volume element approach is implemented to estimate the effective tensile modulus of nanomodified epoxy resins. The results obtained through this homogenization procedure are then used as input for the analysis of nanocomposite fracture toughness, which is carried out by exploiting a classical continuum mechanics-peridynamics coupling strategy. In the coupled model, the small-scale heterogeneity of the crack tip region is preserved by implementing the recently proposed intermediately-homogenized peridynamic model. Comparison to experimental data confirms the capability of the peridynamics-based approaches to properly model the effective tensile modulus and fracture toughness of polymer-based nanocomposites.

Keywords: Polymer/clay nanocomposites, Peridynamics, Experimental analysis, Tensile modulus, Fracture toughness

[*]Corresponding author at: Department of Structural and Geotechnical Engineering, Sapienza University of Rome, v. A. Gramsci 53, Rome 00197, Italy
Email address: `greta.ongaro@uniroma1.it` (Greta Ongaro)

Nomenclature

a	Initial pre-crack length
a_{ij}	Material elastic constants
AR_{mean}, AR_{std}	Mean value and standard deviation of the nanofillers aspect ratio
b	Prescribed body force density field
B	Specimen thickness
$\mathcal{B}$, $\partial\mathcal{B}$	Domain and boundary of the domain
$\mathcal{B}_{FEM}$, $\mathcal{B}_{PD}$	Finite element region and peridynamic region
c	Micromodulus
C	Second-order tensor of **f**
$dV_{\mathbf{x}'}$	Infinitesimal volume associated to the material point $\mathbf{x}'$
$Diff_{rel}$	Relative difference
E	Effective tensile modulus
E_m, E_{nf}, E_{int}, E_{agglm}	Matrix, nanofiller, interface, and agglomeration tensile moduli
f	Pairwise force function
f	Magnitude of **f**
f(x)	Function of the ratio x
G_0	Critical energy release rate
G_{0m}, G_{0nf}, G_{0int}	Critical energy release rates of matrix-matrix, nanofiller-nanofiller, and interface bonds
h	Plate thickness
$\mathcal{H}_{\mathbf{x}}$	Finite neighbourhood of the material point **x**
K_{Ic}	Mode I fracture toughness
K_{Icm}	Average value of the matrix fracture toughness
L_{RVE}	Side length of the square RVE
L_{PDx}, L_{PDy}	Dimensions of the peridynamic region along the x- and y-directions

L_x, L_y	Plate dimensions along the x- and y-directions
m	Ratio between δ and Δx, usually referred to as m-ratio
n	Time step number
p	Spatial dimension
P_{cr}	Peak or fracture load
s, s_0	Scalar bond stretch and critical bond stretch
t	Time
$\mathbf{u}$	Displacement field
u_i	Imposed displacement in the external boundary layers
u_1, u_2	Imposed displacements along the x- and y-directions
vol	Filler volume fraction
V_i	Discretized volume associated to node $\mathbf{x}_i$
wt	Filler weight fraction
W	Specimen ligament
x	Ratio between a and W
x_j	Relative distance of external boundary layer nodes
$\mathbf{x}$	Material point
$\mathbf{x}_i$	Node
$\beta(\boldsymbol{\xi})$	Partial-volume correction factor
γ	Correction factor
δ	Horizon
Δx, Δy	Grid spacings in the x- and y-directions
$\overline{\varepsilon}_{ij}$	Components of the average strain tensor
$\boldsymbol{\eta}$	Relative displacement vector
κ_{int}	Interface factor
$\mu(\boldsymbol{\xi}, t)$	History-dependent scalar-valued function
ν	Effective Poisson's ratio
ν_{DGEBA}	Typical Poisson's ratio for a DGEBA-based epoxy resin
ν_m, ν_{nf}	Matrix and nanofiller Poisson's ratios
$\boldsymbol{\xi}$	Relative position vector in the reference configuration

ρ	Mass density
ρ_m, ρ_{nf}	Matrix and nanofiller volumetric mass densities
$\overline{\sigma}_{ij}$	Components of the average stress tensor
φ	Damage index
χ	Fracture energy factor

1. Introduction

In the last years, the need of the aerospace industry to employ lighter and more efficient components for aircraft, satellite and launcher structures has led to an ever-increasing development of high specific stiffness materials like composites and nanocomposites. Among them, the interest of the academic and industrial communities has been attracted by polymer-based materials reinforced with nanoclay platelets, since they exhibit enhanced mechanical and barrier properties, superior performance in terms of thermal stability and flame retardancy, and excellent corrosion and fatigue resistances [1, 2]. The application of these materials is in fact expanding rapidly in a wide range of fields, such as aerospace, automotive, construction, transportation, and packaging [3, 4].

Nanoclays platelets are characterized by a very large surface area and are exploited to modify polymer materials, due to their unusual mechanical, electrical, optical and magnetic properties, their high availability in nature and low-cost of production [1, 4]. In general, three types of nanoclay morphologies are identified within a polymer matrix, depending on the dispersion state of the silicate layers. These morphologies are referred to as aggregated, intercalated and exfoliated [5]. The molecular interactions between nanoclays and polymer chains lead to a modification of the matrix in the region surrounding the nanofillers. This region is referred to as interface and is usually characterized by properties which can differ substantially from those of both constituents. Considering that this is the zone in which the interactions between the different constituents take place, the properties of this region have a significant influence on the characteristics of the resulting nanocomposite.

The nanocomposite mechanical properties are strongly influenced by the structure of the reinforcing particles and by the quality of their dispersion and distribution within

the polymer material. The inhomogeneous distribution of silicate layers within the matrix leads, in fact, to the formation of local agglomerates, which negatively affect the mechanical performance of the composite [5]. Moreover, the analysis of the relevant literature generally indicates that the addition of low concentrations of nanoclays in a polymer matrix results in a significant enhancement of the tensile properties of the material in well dispersed conditions [6]. For practical applications, the most important property to be studied is the fracture toughness, since nanomodified polymers can be employed as toughened matrices in ternary, fibre reinforced, nanocomposites [7]. Experimental studies available in literature demonstrate that the nanomodification usually enhances the fracture toughness of polymer-based matrices. Furthermore, an aspect which is also highlighted by various studies is the weakening of the mechanical properties which occurs when an optimum clay content is exceeded, due to the formation of various localized agglomerations of nanoclay stacks [4, 7–10].

The numerical modelling of polymer-based nanocomposites is most of the time accomplished using finite element-based techniques [3, 11]. Even though FE-based approaches are widely employed, they present some limitations. For instance, some meshing problems could arise when modelling regions containing particles characterized by an high aspect ratio, i.e., the ratio between nanofillers characteristic length and thickness [11]. Another complexity lies in the modelling of the interface region, since it is the portion of the domain where the stress transfer mechanism takes place, thus requiring a proper selection of element types, geometrical and mechanical properties. The application of these methods for damage prediction also introduces some challenges arising from the presence of spatial derivatives of displacements in the governing equations, which are undefined when the displacement fields are discontinuous [12, Chapter 1]. Many scientists have therefore tried to equip FEM-based models with the capability to simulate crack formation and propagation, but all the proposed strategies present some drawbacks (see [12, Chapter 10]).

Innovative approaches based on the peridynamic (PD) theory have recently been proposed to overcome these limitations. The theory was first introduced in the year 2000 in [13] to model damage and fracture and, since then, it has been extended to a variety of other problems involving the analysis of impact [14, 15], fatigue [16, 17],

5

dynamic fracture [18–22], and sloshing [23]. PD theory has also been exploited for the modelling of several material systems [24–26], and for the study of different physical fields [27–31] and multiphysics problems [32–34]. PD introduces a concept of damage for a material point, allowing to predict the evolution of cracks, including their nucleation and propagation direction, without the need to define any ad hoc criteria or special treatments. The introduction of a length parameter, i.e., the so called horizon, also enables the analysis of material response at different length scales, from macroscale to nanoscale [35], and the implementation of homogenization and multiscale schemes. The growing interest in nanocomposite technologies has in fact given a boost to the development of computational homogenization schemes based on the representative volume element (RVE) or unit cell (UC) concepts. In [36], a PD-based UC model was developed to compute the effective properties of composites through a microstructure informed homogenization scheme. In [37], bond-based PD was employed to develop an RVE-based model to study fibre reinforced composites, whereas, in [38], the RVE concept was exploited to predict polymer-based nanocomposite properties. In the first part of the present work, an RVE-based homogenization is implemented in a PD framework for the modelling of the tensile modulus of polymer/clay nanocomposites. The proposed method, which requires the explicit representation of the material microstructure, has the capability to model randomly distributed curved nanofillers with different sizes and orientations, and to easily simulate interface properties and nanofiller agglomeration phenomena by simply tuning the properties of the PD bonds, therefore not requiring the implementation of multistep homogenization procedures or the definition of equivalent homogenized particles [2, 3, 39]. Moreover, the meshless nature of the proposed method avoids elements distortion issues affecting FEM models dealing with high aspect ratio of nanofillers, hence facilitating the simulation of common high aspect ratio values.

In [40], the authors demonstrate that, in the framework of PD, the implementation of regular homogenization techniques for fracture problems in which the microstructural characteristics play an important role, can fail to represent some experimentally observed behaviours. In order to overcome this limitation, the authors proposed a new homogenization strategy, referred to as intermediately-homogenized peridynamic (IH-

6

PD) model, which enables the modelling of the fracture behaviour without the need for an explicit description of the material microstructure. Inspired by the aforementioned study, in the second part of this work, the IH-PD approach is exploited to study the fracture toughness of polymer-based nanocomposites. Differently from the RVE-based homogenization, this method is applied to simulate the fracture properties of a full scale model of a compact tension specimen [41]. In order to increase the computational efficiency of the model [12, Chapter 14], to avoid the difficulties related to the definition of nonlocal boundary conditions [13], and to eliminate the PD surface effect [18, 42], the IH-PD model is coupled with a FEM-based model by employing the coupling strategy proposed in [43] and [44]. In this way, the area of the domain affected by the presence of discontinuities is described with the IH-PD model, whereas the remaining parts of the domain are represented through a more efficient FEM model.

In the framework of brittle fracture modelling, the bond-based formulation is the standard and most commonly used approach among the PD community, due to its ease of implementation and lower computational cost with respect to the state-based version of the theory. Moreover, the intrinsic Poisson's ratio limitation of bond-based PD is not expected to affect the results and conclusions of the present work, since the Poisson's ratio effect is usually not significant in the fracture behaviour of many materials [45]. The bond-based formulation is therefore exploited here to develop the proposed models.

The numerical approaches are calibrated by using experimental data reported in literature and the experimental results obtained by performing tensile and fracture tests on nanomodified epoxy resins.

The contents of this paper are organized as follows. In Section 2, a brief overview of the bond-based version of PD theory and its discretization are provided. In Section 3, the experimental activity is briefly outlined, focusing on the description of the tensile and mode I fracture tests results in Sections 3.1 and 3.2, respectively. In Section 4, the PD-based RVE approach is presented. Section 5 discusses the coupling-based strategy adopted to study the nanocomposite fracture toughness. Section 6 closes the paper with some remarks and proposals for future research.
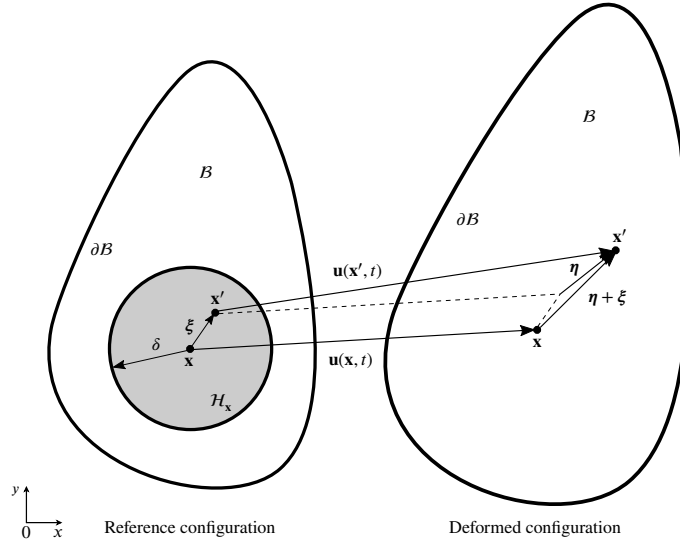
Figure 1: Representation of a generic PD domain $\mathcal{B}$ before and after deformation; the relative position vectors and the relative displacement vector between two material points $\mathbf{x}$ and $\mathbf{x}'$ are also schematically illustrated.

2. Fundamentals of peridynamic theory and its discretization

In a domain $\mathcal{B} \subset \mathbb{R}^p$ with p the spatial dimension, described with a PD model, each material point $\mathbf{x} \in \mathcal{B}$ interacts with all the other material points located within a finite neighbourhood, $\mathcal{H}_{\mathbf{x}}$, of that material point (see Fig. 1). The bond-based PD equation of motion for any material point $\mathbf{x} \in \mathcal{B}$ at time $t \geqslant 0$ is given by [13]:

$$\rho(\mathbf{x})\ddot{\mathbf{u}}(\mathbf{x}, t) = \int_{\mathcal{H}_{\mathbf{x}}} \mathbf{f}\left(\mathbf{u}\left(\mathbf{x}', t\right) - \mathbf{u}\left(\mathbf{x}, t\right), \mathbf{x}' - \mathbf{x}\right) dV_{\mathbf{x}'} + \mathbf{b}(\mathbf{x}, t), \tag{1}$$

where ρ is the mass density, $\ddot{\mathbf{u}}$ is the second derivative in time of the displacement field $\mathbf{u}$, $\mathbf{f}$ denotes the pairwise force function, with units of force per unit volume squared, that the material point $\mathbf{x}'$ exerts on the material point $\mathbf{x}$, and $\mathbf{b}$ is a prescribed body force density field. The neighbourhood $\mathcal{H}_{\mathbf{x}}$ is defined by:

$$\mathcal{H}_{\mathbf{x}} := \{\mathbf{x}' \in \mathcal{B} : \|\mathbf{x}' - \mathbf{x}\| \leqslant \delta\}, \tag{2}$$

where $\delta > 0$ is the horizon. As shown in Fig. 1, the relative position vector of the two material points $\mathbf{x}$ and $\mathbf{x}'$ in the reference configuration is denoted by:

$$\boldsymbol{\xi} := \mathbf{x}' - \mathbf{x}, \tag{3}$$

8

which represents the standard PD notation for a bond. In the deformed configuration at time $t > 0$, the two material points $\mathbf{x}$ and $\mathbf{x}'$ would be displaced, respectively, by $\mathbf{u}(\mathbf{x}, t)$ and $\mathbf{u}(\mathbf{x}', t)$. As schematically represented in Fig. 1, the corresponding relative displacement vector is defined as $\boldsymbol{\eta} := \mathbf{u}(\mathbf{x}', t) - \mathbf{u}(\mathbf{x}, t)$. The force vector $\mathbf{f}$, also called bond force, acts in the direction of the relative position vector of the two material points $\mathbf{x}$ and $\mathbf{x}'$ in the deformed configuration $(\boldsymbol{\eta} + \boldsymbol{\xi})$ (see Fig. 1). The scalar bond stretch s is defined as:

$$s := \frac{\|\boldsymbol{\eta} + \boldsymbol{\xi}\| - \|\boldsymbol{\xi}\|}{\|\boldsymbol{\xi}\|}. \tag{4}$$

In the case of the prototype microelastic brittle (PMB) material model [13], the magnitude f of the force vector $\mathbf{f}$ is given by [14]:

$$f = cs, \tag{5}$$

where c is the micromodulus and represents the bond elastic stiffness. The micromodulus c can be related to measurable macroscopic quantities such as the tensile modulus E and the Poisson's ratio of the material ν (see [14, 46–48]). It is important to highlight that, in bond-based PD, the Poisson's ratio is restricted to a fixed value. For three-dimensional and two-dimensional plane strain cases, the Poisson's ratio is fixed to $\nu = 1/4$, whereas for the two-dimensional plane stress case it is constrained to $\nu = 1/3$ [13, 47]. This limitation has been removed in the state-based version of the theory. The micromoduli for the two-dimensional plane stress and plane strain models presented in this work are computed by employing the correction factor γ introduced in [49]. The concept of material failure is introduced by defining a critical value for the bond stretch, s_0, after which a bond is broken and, consequently, no tensile force can be sustained by the bond (see Fig. 2). The critical stretch s_0 can be related to measurable macroscopic quantities such as the critical energy release rate of the material G_0 (see [14]). As depicted in Fig. 2, the history-dependence of the PMB material constitutive model is introduced by the definition of the function $\mu(\boldsymbol{\xi}, t)$, which can assume either of the following two values:

$$\mu(\boldsymbol{\xi}, t) := \begin{cases} 1 & \text{if } s < s_0 \quad \forall \, 0 < t' < t, \\ 0 & \text{otherwise.} \end{cases} \tag{6}$$
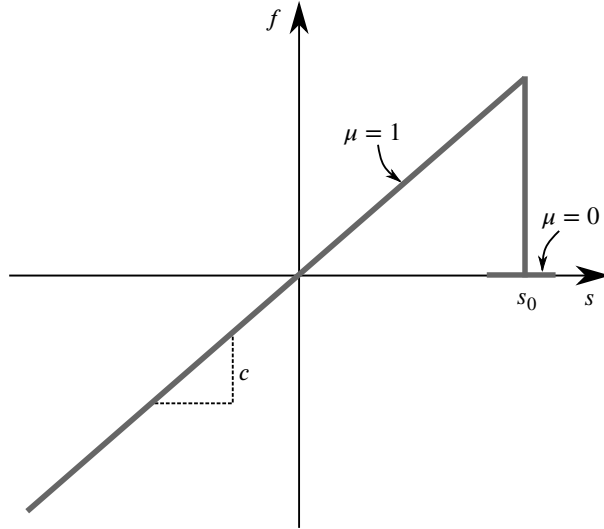
Figure 2: Scalar bond force versus scalar bond stretch for the PMB material model. Redrawn, with modifications, from [14].

This bond-breaking parameter can then be included in the scalar bond force definition, allowing (5) to be rewritten as [13]:

$$f(\boldsymbol{\xi}, t) = \mu(\boldsymbol{\xi}, t)cs. \tag{7}$$

The history-dependence of the constitutive model is a consequence of the fact that the bond breakage is irreversible. The damage level at a material point $\mathbf{x}$ at time t can then be quantified through the damage index φ, which is defined by the following relation:

$$\varphi(\mathbf{x}, t) := 1 - \frac{\int_{\mathcal{H}_{\mathbf{x}}} \mu(\boldsymbol{\xi}, t) dV_{\mathbf{x}'}}{\int_{\mathcal{H}_{\mathbf{x}}} dV_{\mathbf{x}'}}, \tag{8}$$

where $0 \le \varphi \le 1$, 0 represents the undamaged state of the material, and 1 indicates the complete disconnection of the material point $\mathbf{x}$ from all the material points located within its neighbourhood.

The discretized form of the bond-based PD equation of motion can be written by adopting the meshfree approach introduced in [14]:

$$\rho_i \ddot{\mathbf{u}}_i^n = \sum_j \mathbf{f}(\mathbf{u}_j^n - \mathbf{u}_i^n, \mathbf{x}_j - \mathbf{x}_i)\beta(\boldsymbol{\xi})V_j + \mathbf{b}_i^n \quad \forall \mathbf{x}_j \in \mathcal{H}_{\mathbf{x}_i}, \tag{9}$$

10

where i is the index of the central node, j is the family node index and represents all nodes within the neighbourhood $\mathcal{H}_{\mathbf{x}_i}$ of node $\mathbf{x}_i$, n is the time step number, V_j is the discretized volume associated to node $\mathbf{x}_j$, and $\beta(\boldsymbol{\xi})$ is a partial-volume correction factor used to evaluate the portion of V_j that falls within the neighbourhood of the source node $\mathbf{x}_i$, $\mathcal{H}_{\mathbf{x}_i}$ [50]. The spatial integration is performed by adopting the one-point Gauss quadrature rule. In this work, the assumption of small strains and displacements is made, so that, according to [14], the linearized version of (9) can be expressed as:

$$\rho_i \ddot{\mathbf{u}}_i^n = \sum_j \mathbf{C}(\mathbf{x}_j - \mathbf{x}_i)(\mathbf{u}_j^n - \mathbf{u}_i^n)\beta(\boldsymbol{\xi})V_j + \mathbf{b}_i^n \quad \forall \mathbf{x}_j \in \mathcal{H}_{\mathbf{x}_i}, \tag{10}$$

where $\mathbf{C}$ is a second-order tensor of the force vector $\mathbf{f}$ defined by the following relation [13]:

$$\mathbf{C}(\boldsymbol{\xi}) := \frac{\partial \mathbf{f}}{\partial \boldsymbol{\eta}}(0, \boldsymbol{\xi}). \tag{11}$$

The meshfree discretization of the domain implemented in this work considers a uniform distribution of nodes with $\Delta x = \Delta y$, where Δx and Δy are the grid spacings in the x- and y-directions, respectively. A fundamental parameter of the discretized version of PD is the ratio between the horizon and the grid spacing, i.e., $m = \delta/\Delta x$; δ and m are, therefore, the two parameters which determine the number of interactions to be considered for each node in a discretized PD model.

3. Experimental analysis of epoxy/clay nanocomposites

In the present work, a diglycidyl ether of bisphenol A epoxide (DGEBA, Elan-Tech EC157) and the mixture of cycloapliphatic amines (Elan-Tech W152LR), both supplied by Elantas, were used as polymer components. Cloisite®15A, a natural montmorillonite modified with dimethyl dihydrogenated tallow quaternary ammonium salt (Southern Clay Products) was employed for nanomodification. Nanofiller weight fractions of 0%, 1%, 3%, and 5% wt were used to investigate the tensile and fracture properties of the material as a function of the clay content. The samples were prepared according to the procedure described in [8].
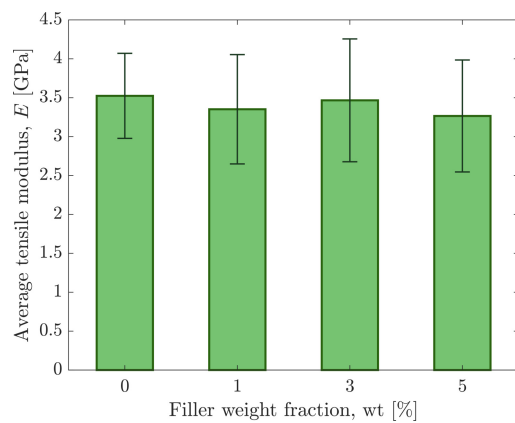
11

Figure 3: Average tensile modulus of the neat epoxy resin and the epoxy/Cloisite®15A nanocomposites with 1%, 3%, and 5% wt of clay content obtained from tensile tests. Error bars: ±1 standard deviation.
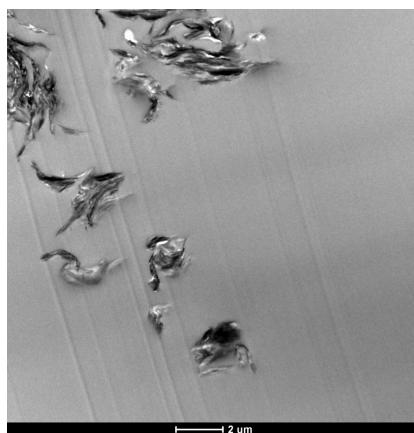

Figure 4: Transmission Electron Microscopy (TEM) image of an epoxy/Cloisite®15A nanocomposite with 5% wt of clay content. The micrograph shows the coexistence between resin-rich areas and nanofiller-rich regions with intercalated and aggregated morphologies.

3.1. Tensile Testing

Tensile tests on dog-bone (DB) specimens were carried out taking advantage of a Galdabini SUN2500 universal mechanical testing machine equipped with a 25 kN load cell using a crosshead speed equal to 2 mm/min. The specimen geometry was chosen according to ISO 527–2 [51]. For each clay content, at least seven specimens were tested to obtain statistically representative results. In all cases, failure took place in the gauge length of the specimens. The experimental results, rearranged according to ISO 527–2 [51], are depicted in Fig. 3 in terms of average values of the tensile modulus and corresponding standard deviations. These data show that the nanomodification of the polymer matrix resulted in a slight decrease in the tensile modulus of the material. The reason for this behaviour lies in the inhomogeneous distribution of nanoclays within the matrix and in the presence of large localized nanofiller aggregates and agglomerated clay stacks (see Fig. 4) [8]. The results reported in Fig. 3 are overall in agreement with previous experimental studies conducted on this class of materials [7, 8].

3.2. Mode I fracture testing

In agreement with the ASTM D5045-14 guidelines [41], mode I fracture tests were carried out on compact tension (CT) specimens by taking advantage of an electro-mechanical testing machine (STEP Lab) equipped with a 10 kN load cell using a crosshead rate of 10 mm/min. The mode I fracture toughness K_{Ic} was computed from the following expression, as suggested by the guidelines reported in ASTM D5045-14 [41]:

$$K_{Ic} = \frac{P_{cr}}{BW^{0.5}} f(x), \tag{12}$$

where P_{cr} is the peak or fracture load measured in [kN], B is the specimen thickness measured in [cm], W is the specimen ligament measured in [cm], $x = \frac{a}{W}$ is the ratio between the initial pre-crack length a and the ligament (see [41]), and the suggested expression for $f(x)$, valid for $0.2 < x < 0.8$, is:

$$f(x) = \frac{(2 + x)\left(0.886 + 4.64x - 13.32x^2 + 14.72x^3 - 5.6x^4\right)}{(1 - x)^{1.5}}. \tag{13}$$

Four values of K_{Ic} were obtained for each clay content, for a total of sixteen samples tested. The results in terms of average values and corresponding standard deviations are
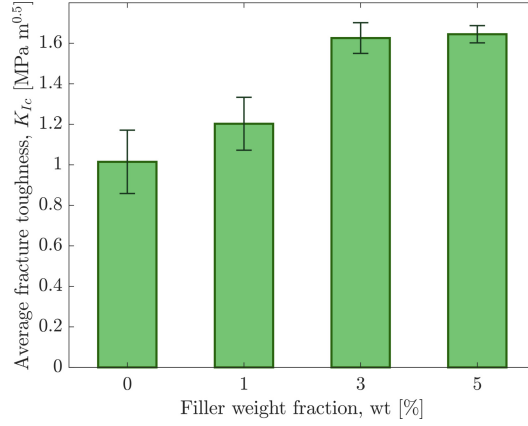
13

Figure 5: Average fracture toughness of the neat epoxy resin and the epoxy/Cloisite®15A nanocomposites with 1%, 3%, and 5% wt of clay content evaluated from mode I fracture tests. Error bars: ±1 standard deviation.

reported in Fig. 5. It is worth mentioning that, as opposed to the tensile modulus (see Fig. 3), the mode I fracture toughness of the epoxy resin was remarkably enhanced by the nanomodification. As shown in Fig. 5, the K_{Ic} had in fact an initial monotonic trend with increasing filler weight fraction, with improvements of about +18.5% and +60.2%

220 as compared with the neat epoxy case for 1% wt and 3% wt of clay content, respectively. The fracture toughness then reached a plateau for 5% wt of nanofiller content, with a slight increase of about +1.2% with respect to the 3% wt case.

The value of the critical energy release rate of the polymer matrix, G_{0m}, which is used as one of the input parameters for the modelling procedure presented in Section 5,

225 can then be computed through the following relation:

$$G_{0m} = \frac{K_{Icm}^2}{E_m}\left(1 - v_{DGEBA}^2\right), \tag{14}$$

where K_{Icm} represents the average value of the fracture toughness of the neat epoxy resin obtained from the fracture tests (see the 0% wt case in Fig. 5), E_m is the average value of the tensile modulus of the neat epoxy resin obtained from the tensile tests (see the 0% wt case in Fig. 3), and v_{DGEBA} is the Poisson's ratio of the matrix material,

230 which is taken here as 0.35 (typical value for a DGEBA-based epoxy resin [9, 52]). This relation is valid under plane strain conditions, as suggested in ASTM D5045-14 [41].

14

The different trends observed for tensile modulus and fracture toughness with increasing filler content are consistent with previous experimental studies reported in literature [7–10], and are related to the morphology of the samples, which are mostly characterized by intercalated and aggregated clay structures (see Fig. 4). Intercalated platelets promote, in fact, the increase of the material toughness, whereas the enhancement of the tensile modulus is usually linked to the presence of exfoliated nanoplatelets [10]. Moreover, it is to note that, some damaging mechanisms previously detected in polymer/clay nanocomposites and comprehensively discussed in [53] were observed here as well through the fracture images reported in Figs. 6 and 7. The presence of intercalated tactoids and microsized filler clusters altered the crack path by inducing crack deflection and pinning. The energy dissipation caused by the crack deflection mechanism was evident from the increase of the fracture surface roughness (see Fig. 6a), whereas crack pinning was identified by the presence of many secondary cracks which tended to unify and form fracture steps, appearing as tails [53] (see Fig. 6b). As shown in Fig. 6c, microvoids were also detected in the regions close to the microsized filler clusters. In addition, microcracks formed via matrix-nanofiller delamination were observed both along the interface region and between the clay platelets (see Figs. 7a and 7b). All the previously mentioned mechanisms were therefore regarded as responsible for the fracture toughness enhancement reported in Fig. 5.

4. PD-based RVE approach for nanocomposite tensile modulus modelling

In the following, an RVE homogenization is implemented in a bond-based PD framework to derive the effective tensile modulus of nanocomposite materials. The results obtained through this numerical procedure are used in the analysis of nanocomposite fracture toughness in Section 5.
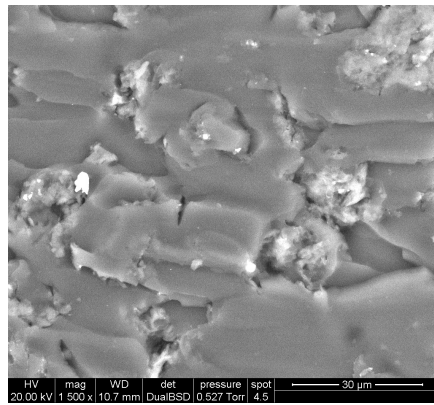
Remark 1. It must be emphasised that the PD models used in Section 4 and Section 5 operate at different length scales. In Section 4, the RVE has a size of $1.5 \times 1.5 \ \mu m^2$ and the nanofillers are individually represented in it. On the contrary, in Section 5, the PD portion of the model has a size of $9.88 \times 6.68 \ mm^2$ and the effect of the nanofillers

15
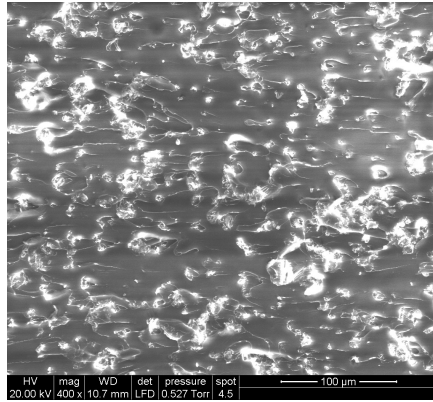
(a)
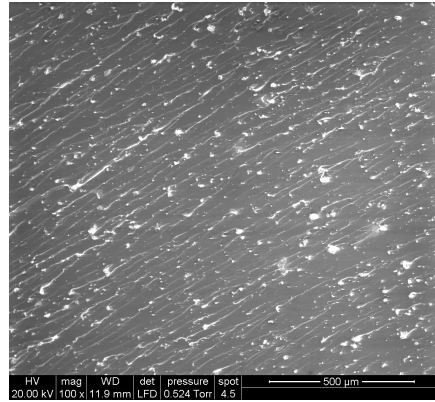
(b)

(c)

Figure 6: Environmental Scanning Electron Microscopy (ESEM) images of epoxy/Cloisite®15A nanocomposites showing (a) crack deflection (5% wt clay-loaded sample), (b) crack pinning (1% wt clay-loaded sample), and (c) microvoids (3% wt clay-loaded sample).
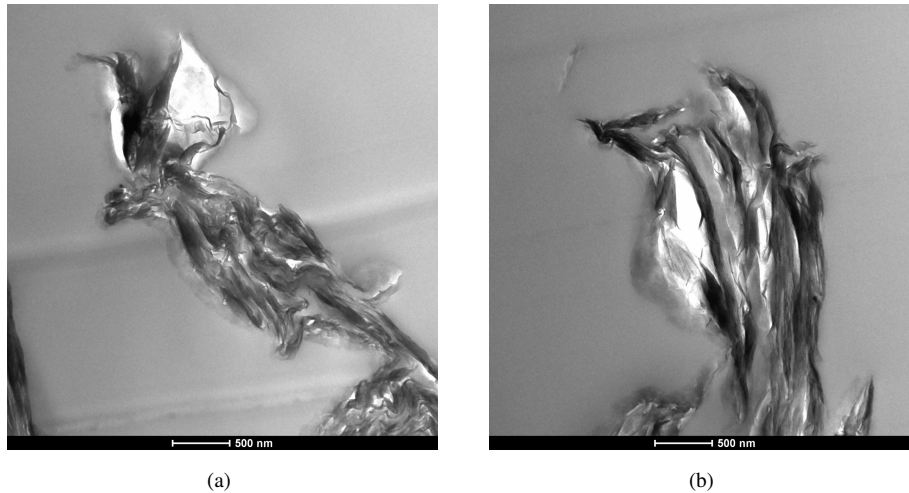
(a) (b)

Figure 7: TEM images of an epoxy/Cloisite®15A nanocomposite sample with 5% wt of clay content.

is introduced only at a statistical level in the definition of the properties of the bonds, according to [40].

4.1. Modelling procedure

Although the PD-based approach proposed in this section could be effectively extended to model three-dimensional RVEs, two-dimensional RVEs are implemented here as a trade-off between accuracy and computational cost. As widely documented in literature [38, 54–57], two-dimensional RVEs have been frequently employed to study polymer/clay nanocomposites, since the relatively small thickness of nanoclay platelets allows for the assumption of a two-dimensional simulation domain under plane stress conditions. As reported in [57], given that the nanoclay has very large length and width, but small thickness, the cross-section of a two-dimensional RVE in fact allows for a good representation of nanoplatelets in a three-dimensional domain.

As comprehensively outlined in [58], different approaches have been developed so far to build RVEs. In this work, the RVE is generated by exploiting an in-house algorithm inspired by the study presented in [55]. Differently from the procedure adopted in [55], the present algorithm allows the overlapping of different nanoplatelets in order to better represent the agglomeration phenomenon.
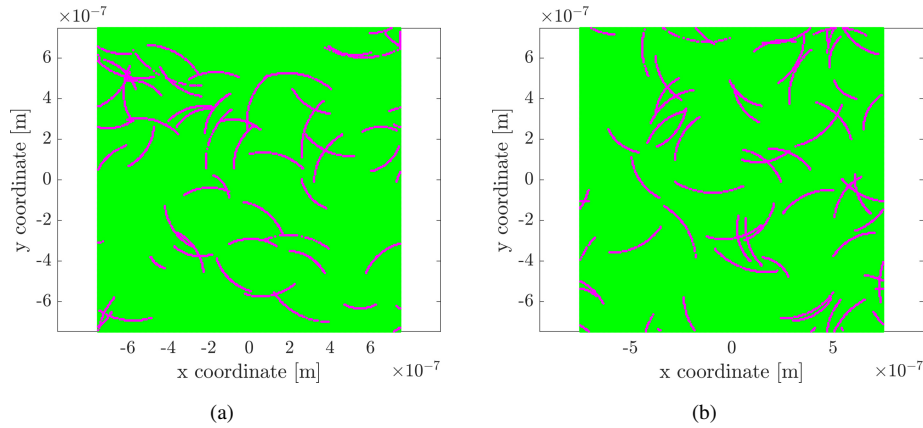
17

Figure 8: Example of two different RVE realizations of the same nanocomposite material. In the geometrically periodic RVEs, the matrix phase is represented by green nodes, whereas the curved nanoclays are represented by magenta nodes.

4.1.1. Definition of nanofiller and matrix properties

Mechanical and geometrical properties of the constituents need to be taken from available experimental studies. In the present work, the required data have been par-

[280] tially obtained from an experimental campaign carried out by the authors (see Section 3.1) and from an experimental investigation reported in literature [52]. In order to take into account the inherently stochastic nature of nanocomposites, the nanofillers aspect ratio, curvature, and location within the matrix are supposed to be affected by uncertainties and therefore modelled by selecting the most suitable probability distribu-

[285] tion functions [55]. The aspect ratio of the nanofillers, AR, is modelled by employing the Gaussian distribution function, whereas discrete uniform distributions are used to model the curvature and location of the nanofillers.

4.1.2. RVE selection and modelling

The properties obtained from available experimental studies are then used as input

[290] for the RVE model [59]. The statistical properties of the nanocomposite are computed by constructing many RVEs, each of them considered as a single realization of the material, and by averaging their results. In order to determine the number of RVEs required to obtain suitable results in terms of effective tensile modulus, it is necessary to study

18

the trend of this property as a function of the number of realizations (see Section 4.2).

Moreover, the RVE should contain a sufficient number of inclusions for the overall moduli to be independent of the surface values of traction and displacement, provided that these values are macroscopically uniform [59].

After the selection of the most suitable size, the square RVE domain is discretized into a grid of PD nodes to which different sets of material properties are assigned to simulate the presence of randomly distributed nanofillers within the matrix. The non-straight shape of the nanofillers is modelled through a newly developed algorithm which also assigns a random aspect ratio and orientation to each nanoplatelet. The domain is modelled as geometrically periodic (see Fig. 8).

Following the allocation of the node properties, the PD bonds are created. Three different types of bonds are defined, depending on the nature of the nodes at their ends: matrix-matrix, nanofiller-nanofiller, and matrix-nanofiller, or interface, bonds. The tensile modulus of the matrix and the one of the nanofiller, i.e., E_m and E_{nf}, are assigned to the matrix-matrix and nanofiller-nanofiller bonds, respectively, while the stiffness of the interface bonds is modelled as a function of the matrix tensile modulus, i.e., $E_{int} = \kappa_{int} E_m$, where κ_{int} represents an interface factor which must be calibrated through available experimental data (see Section 4.2). A special case of nanofiller-nanofiller bonds is represented by the bonds connecting nanofiller-type nodes belonging to different nanoplatelets. The tensile modulus of this subset of bonds, which is employed to simulate the presence of nanoclay agglomerations, is chosen to be equal to the lower between the matrix and interface tensile moduli, depending on each case study, such as:

$$E_{agglm} = \begin{cases} E_m & \text{if } E_{int} \geq E_m, \\ E_{int} & \text{if } E_{int} < E_m. \end{cases} \tag{15}$$

The number of bonds belonging to each of the aforementioned typologies depends on the value of the filler volume fraction, which is referred to as *vol*. In the experimental analysis outlined in Section 3 and, in general, in most experimental studies reported in literature, it is preferred to express the nanoclay content in terms of weight fraction rather than volume fraction. Considering that the numerical approach requires instead

19

the filler content to be defined in terms of volume fraction, it is possible to convert this quantity through the following relation [1]:

$$vol = \frac{\frac{\mathrm{wt}}{\rho_{nf}}}{\frac{\mathrm{wt}}{\rho_{nf}} + \frac{(1-\mathrm{wt})}{\rho_m}},$$ (16)

where ρ_{nf} and ρ_m are the nanofiller and matrix volumetric mass densities, respectively.

4.1.3. Static analysis implementation

Following the definition of the node properties and the creation of the PD bonds, the static analysis implementation is performed. The procedure requires the assembly of the global RVE stiffness matrix and the subsequent application of the boundary conditions, which are imposed on a volume of boundary layers surrounding the RVE domain with a depth equalling the horizon. The implementation of boundary layers makes it possible for all the nodes inside the RVE domain to possess a complete horizon, therefore eliminating the PD surface effect. Displacement boundary conditions are enforced to all the nodes in the external boundary layers. The value of the displacement in the layers is defined through the following relation:

$$u_i = \bar{\varepsilon}_{ij} x_j,$$ (17)

where $\bar{\varepsilon}_{ij}$ are the components of the average strain tensor, and x_j represents the relative distance between the selected node and the centre of the RVE domain, which is located at coordinates $(0,0)$ μm. The material elastic constants are therefore computed by imposing two sets of displacement boundary conditions, i.e., uniaxial strain along x-direction, such that:

$$\begin{cases} \bar{\varepsilon}_{11} \neq 0, \\ \bar{\varepsilon}_{22} = 0, \\ \bar{\varepsilon}_{12} = 0, \end{cases}$$ (18)

and uniaxial strain along y-direction, such that:

$$\begin{cases} \bar{\varepsilon}_{11} = 0, \\ \bar{\varepsilon}_{22} \neq 0, \\ \bar{\varepsilon}_{12} = 0. \end{cases}$$ (19)

20

The two sets of boundary conditions in (18) and (19) are sufficient to obtain the effective tensile modulus and Poisson's ratio of the material. Following the imposition of the boundary conditions, the corresponding reaction forces are computed.

4.1.4. Estimation of the effective material properties

345   The stress-strain relation for macroscopically isotropic materials under plane stress conditions is then employed to evaluate the material elastic constants, a_{ij}, such that:

$$\begin{bmatrix} \overline{\sigma}_{11} \\ \overline{\sigma}_{22} \\ \overline{\sigma}_{12} \end{bmatrix} = \frac{E}{1-v^2} \begin{bmatrix} 1 & v & 0 \\ v & 1 & 0 \\ 0 & 0 & 1-v \end{bmatrix} \begin{bmatrix} \overline{\varepsilon}_{11} \\ \overline{\varepsilon}_{22} \\ \overline{\varepsilon}_{12} \end{bmatrix} = \begin{bmatrix} a_{11} & a_{12} & 0 \\ a_{21} & a_{22} & 0 \\ 0 & 0 & a_{33} \end{bmatrix} \begin{bmatrix} \overline{\varepsilon}_{11} \\ \overline{\varepsilon}_{22} \\ \overline{\varepsilon}_{12} \end{bmatrix}, \quad (20)$$

where $\overline{\sigma}_{ij}$ are the components of the average stress tensor, which is obtained by dividing the sum of the reaction forces computed at the nodes where displacements are imposed by the cross-sectional area of the model, and E and v are the effective tensile modulus and Poisson's ratio of the material, respectively. The elastic constants a_{11} and a_{21} are derived by substituting (18) in (20) and employing the corresponding computed reaction forces, whereas the elastic constants a_{12} and a_{22} are evaluated by substituting (19) in (20) and exploiting the corresponding computed reaction forces. Following the evaluation of the material elastic constants, the tensile modulus and Poisson's ratio, for each of the two load cases considered in this study, are computed by rearranging the system of equations in (20). In the case of a macroscopically homogeneous and isotropic material, such as the one considered in this work, the numerically computed elastic constants should satisfy the following conditions:

$$a_{11} \approx a_{22}, \quad (21a)$$

$$a_{21} \approx a_{12}, \quad (21b)$$

which therefore imply that the numerically computed Poisson's ratios and tensile moduli satisfy the following conditions:

$$v_{21} \approx v_{12} \approx v, \quad (22a)$$

$$E_{11} \approx E_{22} \approx E, \tag{22b}$$

where E_{11} and ν_{21} are the tensile modulus and Poisson's ratio obtained by enforcing the conditions in (18), and E_{22} and ν_{12} are the tensile modulus and Poisson's ratio obtained by imposing the conditions in (19).

350 *4.2. Calibration of the numerical approach*

The proposed approach is calibrated by exploiting the experimental data reported in [52], where the mechanical properties of specimens composed by D.E.R.™ 332, a DGEBA-based epoxy resin from Dow Plastics, nanomodified through the addition of sodium montmorillonite (PGW) from Nanocor Inc. were experimentally investigated. 355 After assessing its capabilities, the numerical approach is employed to numerically compute the effective tensile modulus of the nanocomposite configurations described in Section 3. As mentioned in Section 4.1.2, the proposed strategy implements an interface factor κ_{int} which must be calibrated for each case study to ensure that the properties of the material are properly estimated.

360 *4.2.1. Determination of the suitable RVE size and of the required number of RVE realizations*

In order to define the RVE size, the proposed procedure aims at identifying the minimum side length at which the tensile modulus obtained by imposing a uniaxial strain along x-direction, E_{11}, and the one obtained by imposing the same condition 365 along y-direction, E_{22}, are approximately equal (*cf.* (22b)). The identification of the minimum side length enables the RVE model to contain a sufficient number of randomly distributed inclusions to represent a macroscopically uniform and isotropic material. A set of numerical simulations is therefore performed by keeping constant the value of the filler weight fraction and the properties of the constituents while increasing the side 370 length of the square RVE, i.e., L_{RVE}. Table 1 reports the input data used to carry out the simulations. As for the material properties, the values of E_m, E_{nf}, ρ_m, ρ_{nf}, $\mathrm{AR}_{\mathrm{mean}}$ and $\mathrm{AR}_{\mathrm{std}}$ (i.e., the mean value and standard deviation used to model the nanofillers aspect ratio) are reported in literature studies [52, 55, 60, 61], while the values of ν_m and ν_{nf} are fixed, since plane stress conditions are considered (see Section 2). A test value of

22

Table 1: Input data used to perform the simulations.

Input data	Value
$\Delta x = \Delta y$	10 nm
m	8
E_m	1.96 GPa
E_{nf}	178 GPa
ρ_m	1160 kg/m^3
ρ_{nf}	1980 kg/m^3
$\nu_m = \nu_{nf}$	1/3
AR_{mean}	200
AR_{std}	30

$\kappa_{int} = 10$ and a filler weight fraction of 5% wt are employed in all the simulations. The condition of uniaxial strain along x-direction is enforced by assigning a value of $\overline{\varepsilon}_{11} = 0.01$ to the 11-component of the average strain tensor (*cf.* (18)), whereas the condition of uniaxial strain along y-direction is imposed by assigning a value of $\overline{\varepsilon}_{22} = 0.01$ to the 22-component of the average strain tensor (*cf.* (19)). The study demonstrates that the RVE should be characterized by a side length of at least 1 µm. As reported in Table 2, for $L_{\text{RVE}} < 0.3$ µm, $E_{11} = E_{22} = E_m$, which means that the number of inclusions inside the RVE domain is so low that their presence does not affect the overall material properties, whereas, for $0.3 \leq L_{\text{RVE}} < 1$ µm, E_{11} and E_{22} are quite different from each other, i.e., the condition in (22b) is not satisfied.

As for the required number of RVE realizations, the convergence study aims at identifying the number of RVEs required to obtain suitable results in terms of effective tensile modulus. Table 1 reports the input data used in the simulations, which are per-

Table 2: Results of the study performed to define the suitable RVE size; each case is averaged over 10 runs.

L_{RVE} [µm]	E_{11} [GPa]	E_{22} [GPa]
0.1	1.96 ± 0.03	1.96 ± 0.00
0.15	1.96 ± 0.05	1.96 ± 0.03
0.3	2.58 ± 0.28	2.38 ± 0.10
0.6	2.60 ± 0.10	2.52 ± 0.11
1	2.58 ± 0.09	2.55 ± 0.08
1.5	2.60 ± 0.06	2.58 ± 0.05

formed by employing an RVE side length of $L_{RVE} = 1$ µm, a test value of $\kappa_{int} = 10$, and a filler weight fraction of 5% wt. As reported in Fig. 9, the analysis demonstrates that convergence is guaranteed for approximately 100 realizations with a convergence error of less than 0.05%.

4.2.2. Calibration procedure

The input data used in the calibration procedure are reported in Table 1. An RVE side length of $L_{RVE} = 1.5$ µm is considered in the present study. Each case is averaged over 100 RVE realizations, as suggested by the convergence study presented in Section 4.2.1. The nanofiller weight fractions considered in the calibration procedure are those employed in the experimental investigation carried out in [52], i.e., 0%, 1%, 2.5%, 3.5%, and 5% wt of clay content. The model is calibrated to match the experimentally obtained average value of the tensile modulus of the 5% wt clay-loaded samples. The results shown in Fig. 10 demonstrate that, for $\kappa_{int} = 15$, the model properly predicts the tensile modulus value not only for the 5% wt case, but for all the clay contents considered in the study, with a maximum error of about 4%.

After assessing its capabilities, the proposed PD-based method is exploited to compute the effective tensile modulus of the nanocomposite material described in Section 3.
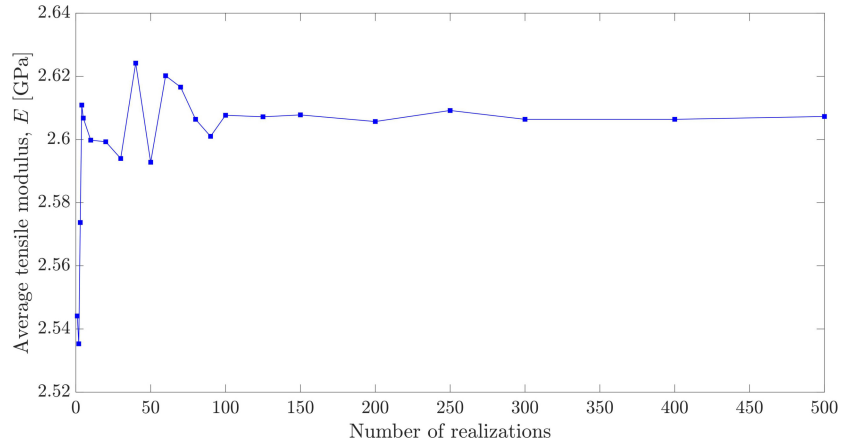
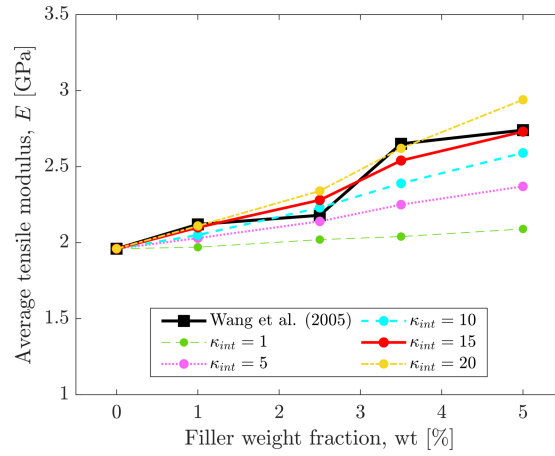Figure 9: Average tensile modulus as a function of RVE realization number.

Figure 10: Calibration of the numerical model to reproduce the experimental results from [52].

Table 3: Numerically computed average tensile modulus for each material configuration considered in Section 3.

Filler weight fraction, wt [%]	E [GPa]
0	3.50 ± 0.00
1	3.46 ± 0.01
3	3.37 ± 0.01
5	3.28 ± 0.02

The nanofiller weight fractions considered in the computations are those employed in the experimental activity outlined in Section 3, i.e., 0%, 1%, 3%, and 5% wt of clay content. The results of the calibration procedure, which are reported in Table 3 in terms of average values of the tensile modulus and corresponding standard deviations, are then used as input parameters for the numerical investigation of nanocomposite fracture toughness presented in Section 5.

5. FEM-PD coupling approach for nanocomposite fracture toughness modelling

In the following, the fracture behaviour of polymer/clay nanocomposites is studied by exploiting the FEM-PD coupling strategy introduced in [43] and [44]. In the first part of the section, the modelling procedure is discussed in detail, while, in the second part, the numerical method is calibrated by exploiting the experimental results reported in Section 3.2.

5.1. Modelling procedure

5.1.1. FEM-PD coupled model generation

A simplified version of the standard CT specimen (see [41]) is modelled to study the fracture toughness of polymer-based nanocomposites as a function of the clay content. The IH-PD model introduced in [40] is employed in the region where the specimen pre-
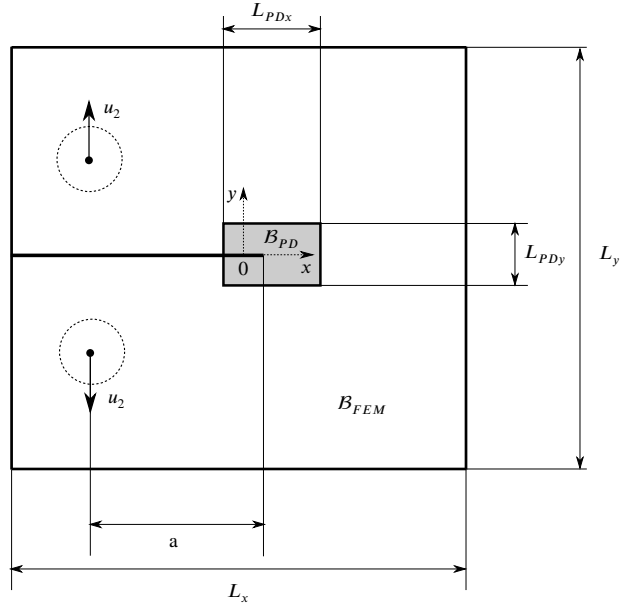
26

Figure 11: FEM-PD coupled model of the CT specimen used to simulate mode I fracture tests.

crack is likely to propagate, whereas the remaining parts of the domain are described using FEM.

In the CT specimen model represented in Fig. 11, the FEM region, $\mathcal{B}_{FEM}$, is mod-
425 elled as fully homogeneous. The effective tensile modulus assigned to the FEM ele-
ments is obtained by exploiting the homogenization approach presented in Section 4.
As for the PD region, $\mathcal{B}_{PD}$, the mechanical properties of the PD bonds are modelled
through the procedure described in [40]. This approach does not require the explicit
representation of the material microstructure, but it just needs information regarding
430 the volume fractions of the material constituents to calibrate the model. The stochas-
tic assignment of the bond properties generates a model which is heterogeneous at the
selected horizon scale, while being homogeneous at larger scales, since the material
is assumed to be macroscopically homogeneous. Therefore, the volume fractions of
the constituents are constant throughout the nanocomposite. Thanks to this innovative
435 approach, small-scale heterogeneity is maintained at a computational cost comparable
to that of commonly used fully homogenized models. The procedure generates three

27

types of bonds: matrix-matrix, nanofiller-nanofiller, and matrix-nanofiller, or interface, bonds. The tensile modulus of the matrix and the one of the nanofiller, i.e., E_m and E_{nf}, are assigned to the matrix-matrix and nanofiller-nanofiller bonds, respectively, while the stiffness of the interface bonds is defined through the harmonic averaging method, as suggested in [40]:

$$E_{int} = \left[\frac{1}{2} \left(E_m^{-1} + E_{nf}^{-1} \right) \right]^{-1}. \tag{23}$$

As for the critical energy release rate values, which are employed for the computation of the critical stretches of the different bonds, the following assumptions are made: the critical energy release rate of the matrix, i.e., G_{0m}, is assigned to the matrix-matrix bonds, whereas the critical energy release rates of the nanofiller-nanofiller and interface bonds are modelled as a function of the matrix fracture energy, such that:

$$G_{0nf} = G_{0int} = \chi G_{0m}, \tag{24}$$

where G_{0nf} and G_{0int} are the critical energy release rates of the nanofiller-nanofiller and interface bonds, respectively, and χ represents a fracture energy factor which must be calibrated through available experimental data to ensure that the fracture toughness of the material is properly estimated (see Section 5.2). Nanofiller-nanofiller bonds therefore possess the stiffness of the nanofiller material, but not its fracture energy, since, under the tensile loading conditions typical of CT fracture tests, only the matrix and the matrix-nanofiller interfaces fail, whereas nanofillers do not break [8, 52].

Following the definition of the properties to be assigned to each kind of bond, the procedure described in [40] is implemented. In the framework of a FEM-PD coupled model, the algorithm proposed in [40] must however be modified to take into account the presence of the coupling zone, which is characterized by bonds connecting PD nodes to FEM nodes to which are assigned the same homogenized properties as the ones allocated to the FEM elements.

5.1.2. Quasi-static solution implementation

Following the creation of the PD bonds, the quasi-static fracture analysis is implemented. The procedure requires the assembly of the coupled stiffness matrix and the

28

subsequent imposition of the boundary conditions. Differently from the RVE model in Section 4, the prescribed displacements do not need to be applied through a finite volume of boundary layers, since the FEM-PD coupled configuration in Fig. 11 enables the use of classical local boundary conditions.

Considering the linear-brittle constitutive behaviour of the PD bonds implemented in this work, a structure subjected to an increasing load has a linear behaviour until the breakage of the first bond. The PD portion of the coupled stiffness matrix needs then to be modified through the removal of the contribution of the broken bond. After this, the structure, characterized by a slightly reduced stiffness, behaves again linearly until the breakage of the next PD bond. This concept is exploited here to implement a sequentially linear analysis (SLA), as discussed in [62]. Fig. 12 shows a typical force-crack mouth opening displacement (CMOD) diagram. Considering that the aim of the modelling approach is to compute the nanocomposite fracture toughness, the procedure can be stopped after the sum of the reaction forces at the nodes where displacements are imposed reaches its peak value, referred to as P_{cr} (*cf.* (12)).

5.2. Calibration of the numerical approach

The proposed approach is calibrated by exploiting the experimental results reported in Section 3.2, where mode I fracture tests were carried out on CT specimens composed by epoxy resin nanomodified through the addition of different weight fractions of montmorillonite Cloisite®15A.

To simulate the mode I fracture tests described in Section 3.2, a simplified CT sample is modelled by using a two-dimensional plate with an internal PD region, as shown in Fig. 11. The PD portion of the domain is a rectangle of edge lengths $L_{PDx} = 9.88$ mm and $L_{PDy} = 6.68$ mm, and its centre has coordinates $(2.4, 0)$ mm. The remaining part of the domain is discretized using four-node square plane strain FEM elements for which the element stiffness matrix has been evaluated with exact integration [63]. The discretization of the domain employs a uniform grid, i.e., $\Delta x = \Delta y$. The values of the plate dimensions and thickness are $L_x = 40.4$ mm, $L_y = 38.8$ mm, and $h = 5$ mm, respectively. A typical initial pre-crack length of a $= 13$ mm is considered in all simulations. The input data used to perform the simulations are reported in Table 4. The

29

Table 4: Input data used to perform the simulations.

Input data	Value
E_m	3.5 GPa
E_{nf}	178 GPa
ρ_m	1156.5 kg/m^3
ρ_{nf}	1660 kg/m^3
$\nu_m = \nu_{nf}$	1/4
G_{0m}	256.4 J/m^2

values of E_m, E_{nf}, ρ_m, and ρ_{nf} have been partially obtained from the experimental activities discussed in Section 3.2 and from experimental investigations reported in literature [55, 60], while the values of ν_m and ν_{nf} are fixed, since plane strain conditions are considered. The value of the critical energy release rate of the matrix, G_{0m}, has been computed through (14). In the simulations, the value of the interface tensile modulus, computed through (23), is $E_{int} = 6.86$ GPa. Moreover, the effective tensile moduli reported in Table 3 are employed to model the stiffness of the FEM elements and of the PD bonds in the coupling zone.

The two-dimensional plate in Fig. 11 is loaded by imposing an upward vertical displacement of $u_2 = 1$ μm on the FEM node located at coordinates $(-12.27, 9.33)$ mm, and a downward vertical displacement of $u_2 = -1$ μm on the FEM node located at coordinates $(-12.27, -9.33)$ mm. In addition, the plate is constrained so that the two aforementioned FEM nodes cannot move in the horizontal direction, i.e., $u_1 = 0$ μm. Using the SLA procedure outlined in Section 5.1.2, the structural problem is solved to obtain the vertical nodal reaction forces of the system, which are then exploited to compute the fracture toughness of the material through (12), where B = h and W = 32.40 mm.

Before proceeding to the calibration phase, a δ-convergence study needs to be per-

formed to investigate the performance of the model and to determine the most suitable horizon size to be employed. The study is carried out by selecting grid spacings of 120, 80, and 60 μm, corresponding to horizon sizes of 480, 320, and 240 μm, respectively. The value of m is chosen as $m = 4$ and is kept fixed during the analysis. The nanofiller weight fraction considered in the convergence study is 0% wt, i.e, the one corresponding to a neat epoxy resin material configuration. The results reported in Table 5 indicate that the material response converges under δ-convergence tests, as expected when dealing with PMB material models for problems with pre-cracks [64]. In light of these results, an horizon of $\delta = 320$ μm and a value of $m = 4$ are selected to carry out the model calibration phase. Fig. 12 shows the force-crack mouth opening displacement diagram obtained for case (b) in Table 5 after performing 5500 steps of the SLA procedure.

The nanofiller weight fractions considered in the calibration procedure are those employed in the experimental investigation described in Section 3, i.e., 0%, 1%, 3%, and 5% wt of clay content. In all simulations, each calculation point is averaged over 5 runs, i.e., over 5 different microstructural realizations of the same material configuration, in order to take into account the stochasticity of the model. The model is calibrated to match the experimentally obtained average value of the fracture toughness of the 3% wt clay-loaded samples (see Fig. 5). The results reported in Fig. 13 demonstrate that, for $\chi = 25$, the model properly predicts the fracture toughness value not only for the 3% wt case, but for all the clay contents considered in the study. Considering that the experimental results reported in Fig. 5 show that, after exceeding a clay content of 3% wt, the average value of the K_{Ic} reached a plateau, the fracture toughness for the 5% wt case is assumed here to be equal to the one computed for the 3% wt case. As previously mentioned, this trend is related to the presence of large localized nanofiller aggregates within the matrix (see Fig. 4), which prevents the fracture toughness to further increase and eventually induces a reduction of its value. The extension of the current model to the simulation of these effects is foreseen for the future. Figs. 14a and 14b show the damage maps obtained after performing 5500 steps of the SLA procedure for the neat epoxy resin case and for one microstructure realization of the epoxy/Cloisite®15A nanocomposite with 3% wt of clay content, respectively. For the neat epoxy case, the model simulate the expected straight crack path, whereas, for the 3% wt case, the het-

31

Table 5: δ-convergence study results.

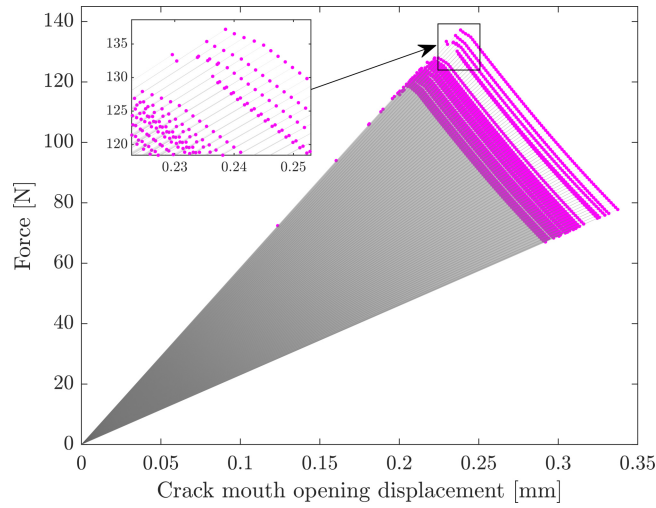| Coupled model, $m = 4$	P_{cr} [N]	$Diff_{rel}$ [%]
Case (a), $\delta = 480$ μm, $\Delta x = 120$ μm	136.05	\
Case (b), $\delta = 320$ μm, $\Delta x = 80$ μm	137.19	0.84
Case (c), $\delta = 240$ μm, $\Delta x = 60$ μm	137.56	0.27

Figure 12: Force-CMOD diagram obtained for case (b) in Table 5 with an enlarged view of the region near the peak value of the reaction force. Magenta circles indicate the bond failure points, while straight grey lines with gradually decreasing slopes represent the progressive reduction of the overall stiffness of the structure.
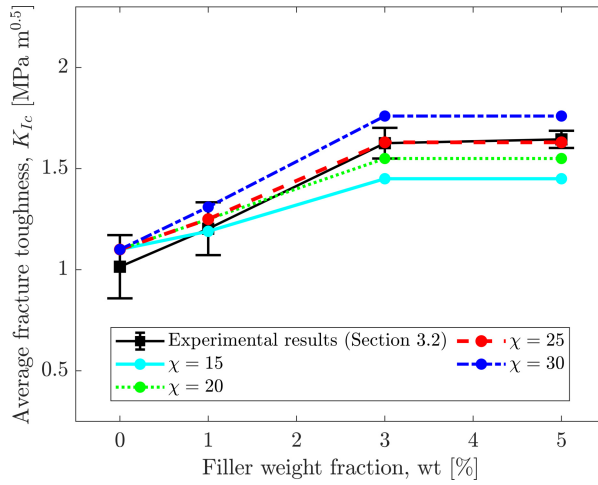
Figure 13: Calibration of the numerical model to reproduce the experimental results from Section 3.2.

erogeneous microstructure stochastically created by the modelling approach enables the reproduction of the experimentally observed crack path tortuosity typical of this class of materials [52].

6. Conclusions

This work concerned the modelling of the mechanical properties of nanocomposite materials. The investigation was particularly focused on polymer-based matrices nanomodified through the addition of nanoclay platelets, a class of materials which has recently attracted the interest of the scientific community due to its enhanced mechanical, thermal, and barrier properties, and to its wide range of applications. A peridynamics-based representative volume element approach was exploited to model the effective tensile modulus of polymer-based nanocomposites. The results of the analysis were then used as input parameters for the numerical investigation of the effect of the nanomodification on the fracture toughness of nanocomposites, which was performed by exploiting a FEM-PD coupling strategy. In the FEM-PD coupled model, the effective tensile moduli obtained through the PD-based RVE approach were used to define the homogenized properties of the FEM region and of the coupling zone. The crack tip region was instead described through an intermediately-homogenized peridynamic

33
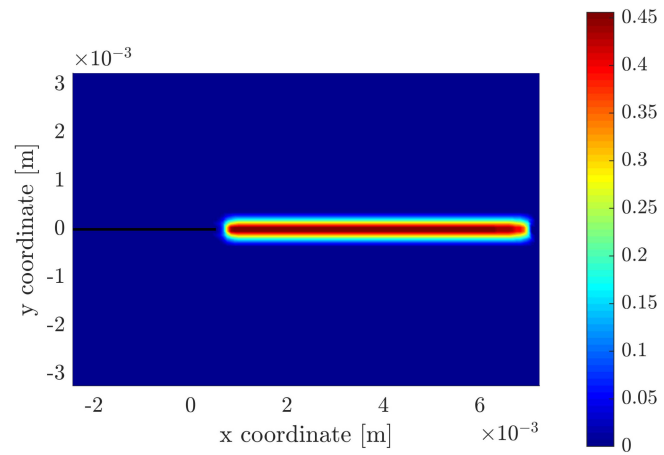
(a)
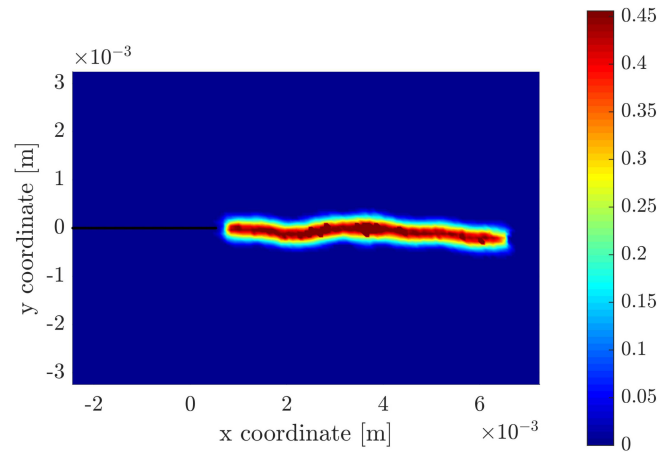
(b)

Figure 14: Damage maps obtained after 5500 steps of the SLA procedure for (a) the neat epoxy resin, and (b) one microstructure realization of the epoxy/Cloisite®15A nanocomposite with 3% wt of clay content. For clarity, only the PD portion of the domain is shown in the figures.

model capable of preserving the small-scale heterogeneity of the material by generating a stochastic microstructure. The proposed computational tools were calibrated by exploiting experimental data available in literature, and by performing tensile and fracture tests on clay-loaded epoxy resins.

CRediT authorship contribution statement

Greta Ongaro: Conceptualization, Methodology, Software, Formal analysis, Investigation, Writing - Original Draft. **Roberta Bertani:** Conceptualization, Validation, Investigation, Resources, Writing - Review & Editing, Supervision. **Ugo Galvanetto:** Conceptualization, Resources, Writing - Review & Editing, Supervision, Funding acquisition. **Alessandro Pontefisso:** Validation, Investigation, Resources. **Mirco Zaccariotto:** Conceptualization, Resources, Writing - Review & Editing, Supervision, Funding acquisition.

Declaration of competing interest

The authors declare that they have no known competing financial interests or personal relationships that could have appeared to influence the work reported in this paper.

Acknowledgements

References

[1] Y. Djebara, A. El Moumen, T. Kanit, S. Madani, A. Imad, Modeling of the effect of particles size, particles distribution and particles number on mechanical properties of polymer-clay nano-composites: Numerical homogenization versus experimental results, Composites Part B: Engineering 86 (2016) 135–142.

[2] V.-H. Nguyen, S. Mahouche-Chergui, B. Carbonnier, S. Naili, et al., Estimation of effective elastic properties of polymer/clay nanocomposites: A parametric study, Composites Part B: Engineering 152 (2018) 139–150.

[3] M. Pahlavanpour, H. Moussaddy, E. Ghossein, P. Hubert, M. Lévesque, Prediction of elastic properties in polymer–clay nanocomposites: Analytical homogenization methods and 3D finite element modeling, Computational materials science 79 (2013) 206–215.

[4] K. J. Shah, A. D. Shukla, D. O. Shah, T. Imae, Effect of organic modifiers on dispersion of organoclay in polymer nanocomposites to improve mechanical properties, Polymer 97 (2016) 525–532.

[5] R. Rafiee, R. Shahzadi, Mechanical Properties of Nanoclay and Nanoclay Reinforced Polymers: A Review, Polymer Composites 40 (2) (2019) 431–445.

[6] S. Pavlidou, C. Papaspyrides, A review on polymer–layered silicate nanocomposites, Progress in polymer science 33 (12) (2008) 1119–1198.

[7] M. Quaresimin, R. Bertani, M. Zappalorto, A. Pontefisso, F. Simionato, A. Bartolozzi, Multifunctional polymer nanocomposites with enhanced mechanical and anti-microbial properties, Composites Part B: Engineering 80 (2015) 108–115.

[8] A. Bartolozzi, R. Bertani, E. Burigo, A. Fabrizi, F. Panozzo, M. Quaresimin, F. Simionato, P. Sgarbossa, S. Tamburini, M. Zappalorto, et al., Multifunctional Cu^{2+}-montmorillonite/epoxy resin nanocomposites with antibacterial activity, Journal of Applied Polymer Science 134 (16) (2017).

36

[9] M. Zappalorto, M. Salviato, M. Quaresimin, Mixed mode (I + II) fracture toughness of polymer nanoclay nanocomposites, Engineering Fracture Mechanics 111 (2013) 50–64.

[10] C. Zilg, R. Mülhaupt, J. Finter, Morphology and toughness/stiffness balance of nanocomposites based upon anhydride-cured epoxy resins and layered silicates, Macromolecular Chemistry and Physics 200 (3) (1999) 661–670.

[11] P. Bian, S. Schmauder, H. Qing, Strength and damage of nanoplatelets reinforced polymer: A 3D finite element modeling and simulation, Composite Structures 245 (2020) 112337.

[12] F. Bobaru, J. T. Foster, P. H. Geubelle, S. A. Silling (Eds.), Handbook of Peridynamic Modeling, CRC Press, 2016.

[13] S. A. Silling, Reformulation of elasticity theory for discontinuities and long-range forces, Journal of the Mechanics and Physics of Solids 48 (1) (2000) 175–209.

[14] S. A. Silling, E. Askari, A meshfree method based on the peridynamic model of solid mechanics, Computers & Structures 83 (17-18) (2005) 1526–1535.

[15] J. Xu, A. Askari, O. Weckner, S. Silling, Peridynamic analysis of impact damage in composite laminates, Journal of Aerospace Engineering 21 (3) (2008) 187–194.

[16] S. A. Silling, A. Askari, Peridynamic model for fatigue cracking, SAND2014-18590. Albuquerque: Sandia National Laboratories (2014).

[17] M. Zaccariotto, F. Luongo, G. Sarego, D. Dipasquale, U. Galvanetto, Fatigue Crack Propagation with Peridynamics: a sensitivity study of Paris law parameters, CEAS2013, Innov Eur Sweden, Linkoping (2013).

[18] Y. D. Ha, F. Bobaru, Characteristics of dynamic brittle fracture captured with peridynamics, Engineering Fracture Mechanics 78 (6) (2011) 1156–1168.

[19] A. Shojaei, T. Mudric, M. Zaccariotto, U. Galvanetto, A coupled meshless finite point/peridynamic method for 2D dynamic fracture analysis, International Journal of Mechanical Sciences 119 (2016) 419–431.

37

[20] A. Shojaei, F. Mossaiby, M. Zaccariotto, U. Galvanetto, An adaptive multi-grid peridynamic method for dynamic fracture analysis, International Journal of Mechanical Sciences 144 (2018) 600–617.

[21] S. Silling, Dynamic fracture modeling with a meshfree peridynamic code, In: Computational Fluid and Solid Mechanics 2003, Elsevier, (2003) 641–644.

[22] F. Mossaiby, P. Sheikhbahaei, A. Shojaei, Multi-adaptive coupling of finite element meshes with peridynamic grids: robust implementation and potential applications, Engineering with Computers (2022) 1–22.

[23] S. Bazazzadeh, A. Shojaei, M. Zaccariotto, U. Galvanetto, Application of the peridynamic differential operator to the solution of sloshing problems in tanks, Engineering Computations (2018).

[24] S. Bazazzadeh, F. Mossaiby, A. Shojaei, An adaptive thermo-mechanical peridynamic model for fracture analysis in ceramics, Engineering Fracture Mechanics 223 (2020) 106708.

[25] W. Gerstle, N. Sau, S. Silling, Peridynamic modeling of concrete structures, Nuclear engineering and design 237 (12-13) (2007) 1250–1258.

[26] E. Oterkus, E. Madenci, Peridynamic analysis of fiber-reinforced composite materials, Journal of Mechanics of Materials and Structures 7 (1) (2012) 45–84.

[27] F. Bobaru, M. Duangpanya, The peridynamic formulation for transient heat conduction, International Journal of Heat and Mass Transfer 53 (19-20) (2010) 4047–4059.

[28] A. Hermann, A. Shojaei, D. Steglich, D. Höche, B. Zeller-Plumhoff, C. J. Cyron, Combining peridynamic and finite element simulations to capture the corrosion of degradable bone implants and to predict their residual strength, International Journal of Mechanical Sciences (2022) 107143.

[29] S. Jafarzadeh, A. Larios, F. Bobaru, Efficient solutions for nonlocal diffusion problems via boundary-adapted spectral methods, Journal of Peridynamics and Nonlocal Modeling (2020) 1–26.

38

[30] A. Shojaei, A. Hermann, P. Seleson, C. J. Cyron, Dirichlet absorbing boundary conditions for classical and peridynamic diffusion-type models, Computational Mechanics 66 (4) (2020) 773–793.

[31] A. Shojaei, A. Hermann, C. J. Cyron, P. Seleson, S. A. Silling, A hybrid mesh-free discretization to improve the numerical performance of peridynamic models, Computer Methods in Applied Mechanics and Engineering 391 (2022) 114544.

[32] S. Bazazzadeh, M. Morandini, M. Zaccariotto, U. Galvanetto, Simulation of chemo-thermo-mechanical problems in cement-based materials with peridynamics, Meccanica (2021) 1–23.

[33] V. Diana, V. Carvelli, An electromechanical micropolar peridynamic model, Computer Methods in Applied Mechanics and Engineering 365 (2020) 112998.

[34] S. Jafarzadeh, Z. Chen, S. Li, F. Bobaru, A peridynamic mechano-chemical damage model for stress-assisted corrosion, Electrochimica Acta 323 (2019) 134795.

[35] E. Askari, F. Bobaru, R. Lehoucq, M. Parks, S. Silling, O. Weckner, Peridynamics for multiscale materials modeling, In: Journal of Physics: Conference Series, Vol. 125, IOP Publishing, (2008) 012078.

[36] E. Madenci, A. Barut, N. D. Phan, Peridynamic unit cell homogenization, In: 58th AIAA/ASCE/AHS/ASC Structures, Structural Dynamics, and Materials Conference, (2017) 1138.

[37] W. Xia, Y. K. Galadima, E. Oterkus, S. Oterkus, Representative volume element homogenization of a composite material by using bond-based peridynamics, Journal of Composites and Biodegradable Polymers 7 (2019) 51–56.

[38] M. Duzzi, M. Zaccariotto, U. Galvanetto, Application of peridynamic theory to nanocomposite materials, In: Advanced Materials Research, Vol. 1016, Trans Tech Publ, (2014) 44–48.

[39] Y. Zare, K. Y. Rhee, Multistep modeling of Young's modulus in polymer/clay nanocomposites assuming the intercalation/exfoliation of clay layers and the in-

39

terphase between polymer matrix and nanoparticles, Composites Part A: Applied Science and Manufacturing 102 (2017) 137–144.

[40] Z. Chen, S. Niazi, G. Zhang, F. Bobaru, Peridynamic Functionally Graded and Porous Materials: Modeling Fracture and Damage, Handbook of Nonlocal Continuum Mechanics for Materials and Structures (2017) 1–35.

[41] Standard Test Methods for Plane-Strain Fracture Toughness and Strain Energy Release Rate of Plastic Materials, Standard, American Society for Testing and Materials International (2014).

[42] F. Scabbia, M. Zaccariotto, U. Galvanetto, A novel and effective way to impose boundary conditions and to mitigate the surface effect in state-based peridynamics, International Journal for Numerical Methods in Engineering 122 (20) (2021) 5773–5811.

[43] U. Galvanetto, T. Mudric, A. Shojaei, M. Zaccariotto, An effective way to couple FEM meshes and peridynamics grids for the solution of static equilibrium problems, Mechanics Research Communications 76 (2016) 41–47.

[44] M. Zaccariotto, T. Mudric, D. Tomasi, A. Shojaei, U. Galvanetto, Coupling of FEM meshes with peridynamic grids, Computer Methods in Applied Mechanics and Engineering 330 (2018) 471–497.

[45] F. Delale, F. Erdogan, The crack problem for a nonhomogeneous plane (1983).

[46] F. Bobaru, M. Yang, L. F. Alves, S. A. Silling, E. Askari, J. Xu, Convergence, adaptive refinement, and scaling in 1D peridynamics, International Journal for Numerical Methods in Engineering 77 (6) (2009) 852–877.

[47] W. Gerstle, N. Sau, S. Silling, Peridynamic modeling of plain and reinforced concrete structures, SMiRT 18 (2005) 54–68.

[48] Y. D. Ha, F. Bobaru, Studies of dynamic crack propagation and crack branching with peridynamics, International Journal of Fracture 162 (1) (2010) 229–244.

40

[49] G. Ongaro, P. Seleson, U. Galvanetto, T. Ni, M. Zaccariotto, Overall equilibrium in the coupling of peridynamics and classical continuum mechanics, Computer Methods in Applied Mechanics and Engineering 381 (2021) 113515.

[50] P. Seleson, Improved one-point quadrature algorithms for two-dimensional peridynamic models based on analytical calculations, Computer Methods in Applied Mechanics and Engineering 282 (2014) 184–217.

[51] Plastics. Determination of tensile properties. Part 2: Test Conditions for Moulding and Extrusion Plastics, Standard, International Organization for Standardization (2012).

[52] K. Wang, L. Chen, J. Wu, M. L. Toh, C. He, A. F. Yee, Epoxy Nanocomposites with Highly Exfoliated Clay: Mechanical Properties and Fracture Mechanisms, Macromolecules 38 (3) (2005) 788–800.

[53] M. Quaresimin, K. Schulte, M. Zappalorto, S. Chandrasekaran, Toughening mechanisms in polymer nanocomposites: From experiments to modelling, Composites Science and Technology 123 (2016) 187–204.

[54] J. Decklever, P. Spanos, Nanocomposite material properties estimation and fracture analysis via peridynamics and Monte Carlo simulation, Probabilistic Engineering Mechanics 44 (2016) 77–88.

[55] M. Silani, H. Talebi, S. Ziaei-Rad, P. Kerfriden, S. P. Bordas, T. Rabczuk, Stochastic modelling of clay/epoxy nanocomposites, Composite Structures 118 (2014) 241–249.

[56] Y. Dong, D. Bhattacharyya, A simple micromechanical approach to predict mechanical behaviour of polypropylene/organoclay nanocomposites based on representative volume element (RVE), Computational materials science 49 (1) (2010) 1–8.

[57] L. Zhu, K. Narh, Numerical simulation of the tensile modulus of nanoclay-filled polymer composites, Journal of Polymer Science Part B: Polymer Physics 42 (12) (2004) 2391–2406.

41

[58] L. Maragoni, P. Carraro, M. Quaresimin, Development, validation and analysis of an efficient micro-scale representative volume element for unidirectional composites, Composites Part A: Applied Science and Manufacturing 110 (2018) 268–283.

[59] R. Hill, Elastic properties of reinforced solids: Some theoretical principles, Journal of the Mechanics and Physics of Solids 11 (5) (1963) 357–372.

[60] B. Chen, J. R. Evans, Elastic moduli of clay platelets, Scripta materialia 54 (9) (2006) 1581–1585.

[61] J.-J. Luo, I. M. Daniel, Characterization and modeling of mechanical behavior of polymer/clay nanocomposites, Composites science and technology 63 (11) (2003) 1607–1616.

[62] T. Ni, M. Zaccariotto, Q.-Z. Zhu, U. Galvanetto, Static solution of crack propagation problems in peridynamics, Computer Methods in Applied Mechanics and Engineering 346 (2019) 126–151.

[63] O. C. Zienkiewicz, R. L. Taylor, The Finite Element Method: Solid Mechanics, Vol. 2, Butterworth-Heinemann, 2000.

[64] S. Niazi, Z. Chen, F. Bobaru, Crack nucleation in brittle and quasi-brittle materials: A peridynamic analysis, Theoretical and Applied Fracture Mechanics 112 (2021) 102855.

42